

Virtual testing of dual-phase steels: Effect of martensite morphology on plastic flow behavior

J. Pagenkopf^{a,b,*}, A. Butz^a, M. Wenk^c, D. Helm^a,

^a*Fraunhofer Institute for Mechanics of Materials IWM, 79108 Freiburg, Germany*

^b*Karlsruhe Institute of Technology, Institute for Applied Materials, 76131 Karlsruhe, Germany*

^c*Karlsruhe Institute of Technology, Institute for Applied Materials, 76344 Eggenstein-Leopoldshafen, Germany*

Abstract

Dual-phase steels exhibit a moderate plastic anisotropy as a result of the underlying microstructure. A numerical homogenization scheme based on full-field finite element simulations was applied to assess the effect of the martensite morphology on the stress-strain curves and the plastic strain ratios (r-values) of a dual-phase steel under uniaxial tensile loading in different directions. The simulation results show that the martensite morphology affects the macroscopic response and the degree of plastic anisotropy. The mechanical behavior of the dual-phase steel (DP600) investigated in this work could be predicted if the crystallographic texture of the material and a statistically equivalent martensite morphology were considered in the simulations. The corresponding finite element models of the dual-phase microstructure were generated using a reconstruction procedure based on statistical correlation functions. This study demonstrates that the predictive capabilities of

*Corresponding author

Email address: jan.pagenkopf@iwm.fraunhofer.de (J. Pagenkopf)

the virtual testing approach strongly depend on the level of detail with which the microstructural features are represented in the simulations.

Keywords:

Dual-phase steel, Plastic anisotropy, Microstructure reconstruction,
Numerical homogenization, Crystal plasticity, Finite element method

1. Introduction

The characteristic properties like continuous yielding and the favorable combination of high strength and good ductility make dual-phase (DP) steels widely used in industrial applications [1]. The microstructure of this type of steel is composed of hard martensite particles embedded in a soft ferrite matrix. By changing the characteristics of the microstructure constituents, the strength and formability can be varied in a broad range. Thus, it is of great importance to understand the underlying structure-property relations. Numerical simulations based on a spatially resolved representation of the microstructure are frequently applied to study the mechanical behavior of dual-phase steels. Such full-field simulation approaches are often performed using the finite element method or spectral methods as the numerical framework to solve for the local stress and strain fields. The simulation results depend on the representation of the microstructure and the constitutive description of the individual phases. A variety of approaches that differ considerably regarding the level of detail used for the incorporation of microstructural features can be found in the literature (see [2] for a comprehensive overview). For example, different combinations of constitutive models were used in previous works: isotropic plasticity models for both phases [3, 4, 5, 6],

a combination of an isotropic plasticity model for martensite and a crystal plasticity model for ferrite [7] or crystal plasticity models for both phases [8, 9, 10, 11]. Numerous studies were performed with a two-dimensional representation of the dual-phase steel microstructure to study microscale effects like strain localization [12, 4, 13] or to predict the macroscopic strain hardening behavior [14, 3, 15]. In contrast to three-dimensional simulations, this approach reduces computational costs and allows to directly use the real microstructure obtained from micrographs as the simulation domain. Although three-dimensional models of DP microstructures have been generated based on experimental data by using statistical methods [16], most simulations use a simplified and idealized representation of microstructural features like the martensite morphology [8, 6, 10].

However, virtual testing strategies based on numerical homogenization schemes require three-dimensional models with a suitable level of detail regarding the microstructure representation for a comprehensive prediction of material properties. Although virtual testing approaches using full-field simulations have been applied to predict the effective mechanical behavior of single-phase sheet metals [17, 18, 19], they have not been used to predict the anisotropic properties of DP structures. Since dual-phase steels are commonly used as sheet metals, the shape of the yield surface and the r -values are important for the analysis of sheet forming applications in order to predict geometries, thinning and springback. To account for the plastic anisotropy of dual-phase steels in macroscopic plasticity models, different yield functions like Hill'48 or Yld2000-2d have been used [20, 21, 22]. Fig. 1 shows a comparison between r -values of DP600 steels taken from the literature [20, 23, 24, 21, 25]. Differ-

ent trends regarding the direction dependence of the plastic strain ratio were reported for this type of steel. Apart from possible differences due to the applied measurement techniques, this behavior can be explained by a strong dependence of the r -values on the particular microstructure and processing history.

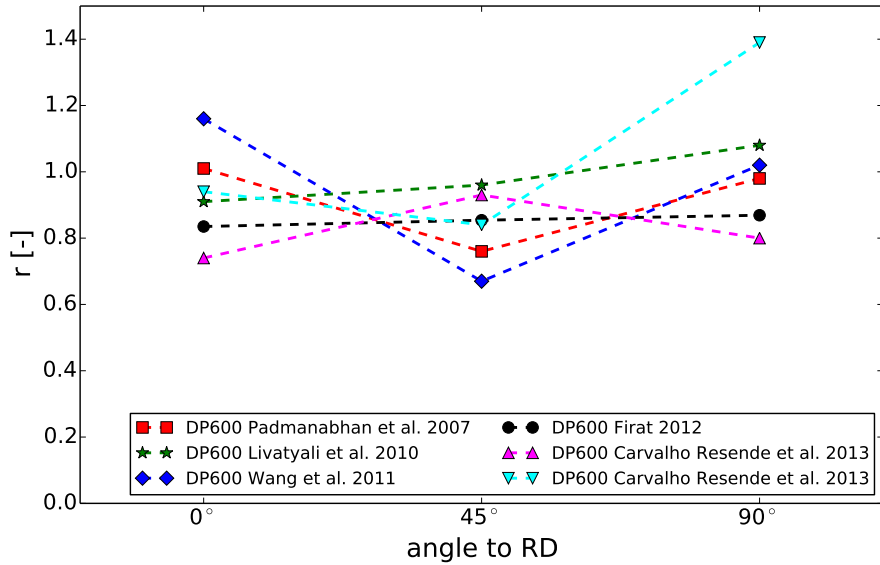


Figure 1: Comparison of r -values measured for different DP600 steels taken from the literature.

So far, the r -values of dual-phase steels have been related to the crystallographic texture of the material [26, 27]. However, [28] pointed out that using a viscoplastic self-consistent (VPSC) polycrystal model to predict the r -values resulted in an overestimation of the plastic strain ratios since the effect of the martensite phase was neglected. In fact, it is difficult to incorporate a detailed description of the martensite morphology into mean-field

models. This microstructural feature is often neglected even if only the strain hardening behavior of dual-phase steels is modeled [29, 30, 31].

In the present work, a numerical homogenization scheme based on three-dimensional full-field simulations using the finite element method was applied to assess the dependence of the anisotropic plastic flow behavior on different microstructural features. In particular, the effect of the martensite morphology was investigated. First, a numerical study was conducted to compare the effect of different martensite morphologies on the effective material behavior in terms of stress-strain curves and r-values. In the second step, a reconstruction procedure based on microstructural correlation functions as proposed by [32, 33] was used to generate microstructure models with a martensite morphology that is statistically equivalent to the real material. The predicted material behavior obtained from simulations with these models was compared with experimental results. In addition, the effect of the mechanical phase contrast on the predicted r-values was investigated.

2. Material characterization

2.1. Microstructure analysis

DP600 steel sheets with a thickness of $t = 1.0$ mm were investigated in the as-received condition, i.e. after cold-rolling and intercritical annealing. The chemical composition was measured via spark-emission spectrometry and is given in Table 1.

Optical micrographs taken from the middle of the sheet for cross sections orthogonal to the rolling direction (RD) and orthogonal to the transverse direction (TD) are shown in Fig. 2. The morphology of the martensite phase

Table 1: Chemical composition of DP600 (in wt.%).

C	Si	Mn	P	S	Cu	Cr	Ni	Al	V
0.093	0.29	1.663	0.011	0.001	0.029	0.341	0.047	0.046	0.001

was revealed using a Nital etchant. Based on the microstructure observation, a martensite content of $V^{(m)} = 12\%$ was identified. The micrographs provide the statistical information that are needed for the reconstruction process of the martensite phase described in Section 3.

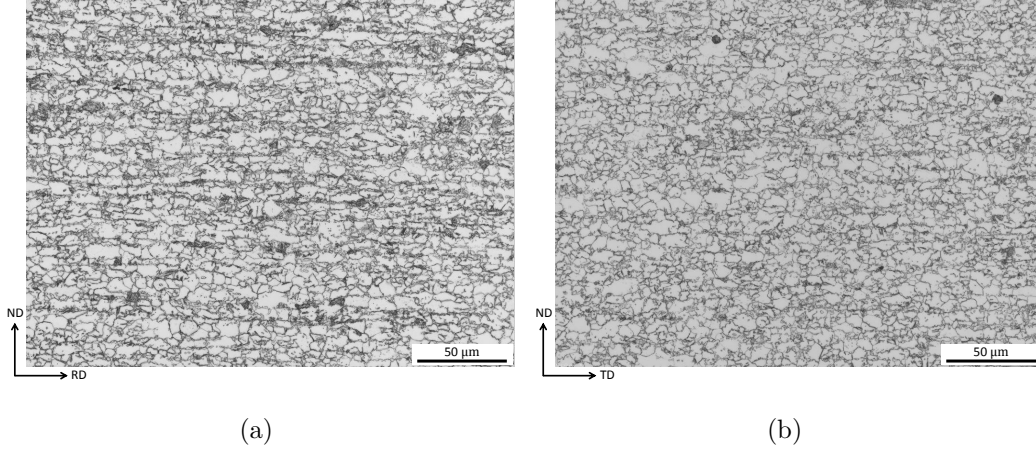


Figure 2: Micrographs taken from cross sections (a) orthogonal to the transverse direction and (b) orthogonal to the rolling direction.

In addition, the crystallographic texture of the material and the grain size of the ferrite matrix were analyzed based on electron backscatter diffraction (EBSD) measurements. Fig. 3 (a) shows the EBSD map for an area of $150\text{ }\mu\text{m} \times 600\text{ }\mu\text{m}$ with a step size of $0.5\text{ }\mu\text{m}$. The scan area is located in the middle of the sheet and contains approximately 5800 ferrite grains. The pole figure representation of the orientation distribution function (ODF) that was

calculated from the orientation information using the MTEX toolbox [34] is shown in Fig. 3 (b).

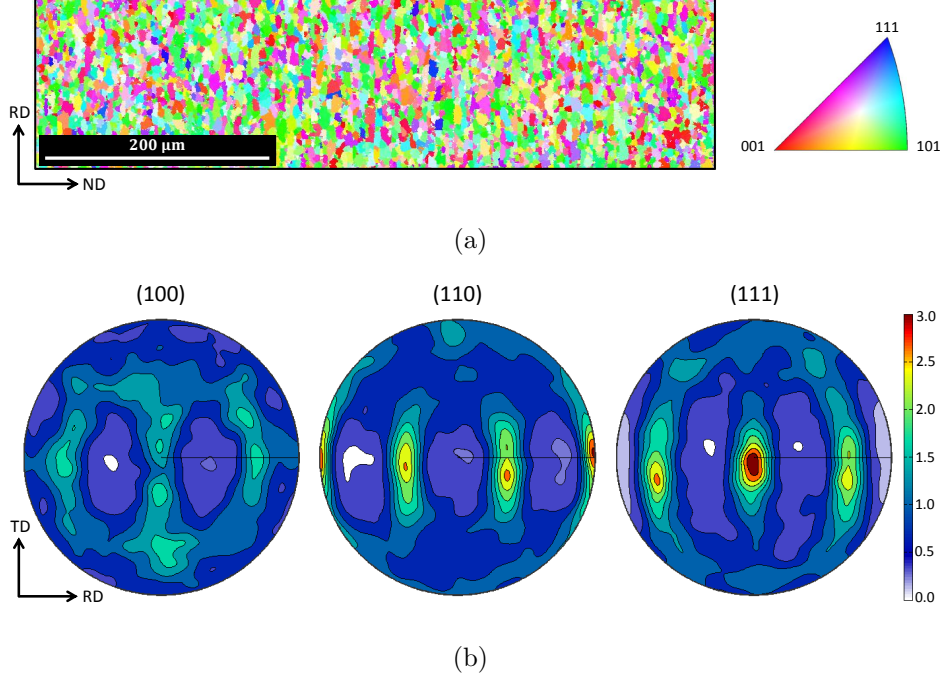


Figure 3: Results from EBSD scan with a step size of $0.5\text{ }\mu\text{m}$: (a) EBSD map and (b) pole figure representation of the crystallographic texture.

For the ferrite grains, an average equivalent area diameter of $d^{(f)} = 3.1\text{ }\mu\text{m}$ was determined based on EBSD measurements with a higher resolution using a step size of $0.125\text{ }\mu\text{m}$. Here, the phases could be separated due to the low band contrast of the martensite islands.

2.2. Mechanical testing

Uniaxial tensile tests were carried out in three directions (0° , 45° and 90° to RD) with a strain rate of 0.0005 s^{-1} . The results of these tests that are used in the following are taken from [35]. The stress-strain curves are shown in

Fig. 4 and indicate a nearly isotropic behavior regarding the yield stress and the hardening of the material.

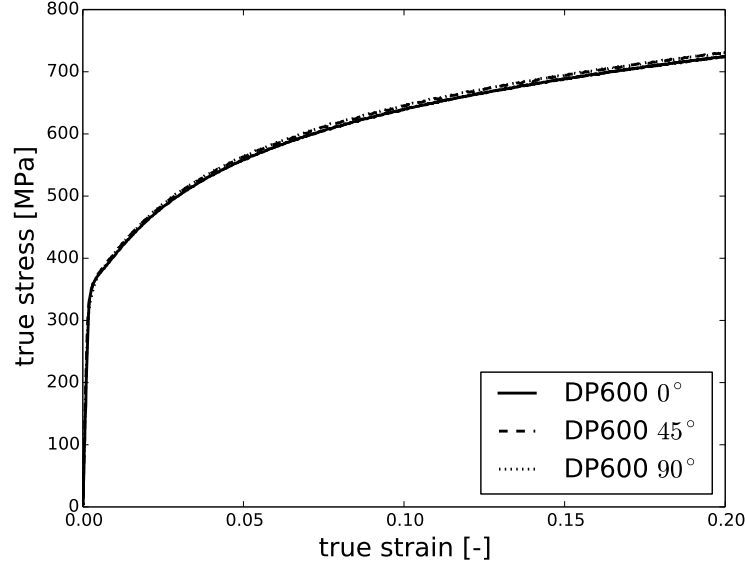


Figure 4: Stress-strain curves obtained from tensile tests in three different directions with respect to the rolling direction (data taken from [35]).

In addition, the strains in longitudinal and width direction were measured using an optical strain measurement system to obtain the r-values. The r-value (or Lankford coefficient) is defined as the ratio of the true plastic strains in width and thickness direction according to

$$r = \frac{\varepsilon_w^{\text{pl}}}{\varepsilon_t^{\text{pl}}}. \quad (1)$$

Since $\varepsilon_l^{\text{pl}} + \varepsilon_w^{\text{pl}} + \varepsilon_t^{\text{pl}} = 0$ holds for the plastic strains in longitudinal, width and thickness direction, the r-value can be calculated from the strains in longitudinal and width direction using

$$r = \frac{\varepsilon_w^{\text{pl}}}{-(\varepsilon_l^{\text{pl}} + \varepsilon_w^{\text{pl}})} = -\frac{m}{1+m} \quad (2)$$

with $m = \varepsilon_w^{\text{pl}}/\varepsilon_l^{\text{pl}}$. The experimental r -values obtained from fitting the parameter m to the $\varepsilon_w^{\text{pl}}(\varepsilon_l^{\text{pl}})$ plot for tensile strains between 5 % and 15 % are listed in Table 2.

Table 2: Experimental r -values for DP600 obtained from uniaxial tensile tests (data taken from [35]).

	Specimen 1	Specimen 2	Specimen 3	Average
$r_{0/5-15}$	0.88	0.88	0.89	0.88
$r_{45/5-15}$	0.88	0.90	0.90	0.89
$r_{90/5-15}$	1.05	1.06	1.05	1.05

The DP600 exhibits a moderate anisotropy regarding the plastic strain ratios and an average normal anisotropy of $r_m = (r_0 + 2r_{45} + r_{90})/4 = 0.93$ which is typical for dual-phase steels.

3. Generation of microstructure models

This section describes the generation of the microstructure models that were used to perform numerical simulations with the finite element software package Abaqus/Standard. In a first step, finite element models with different martensite morphologies were generated. These models are referred to as concept microstructure models (CMM) and were used for a numerical study to assess the effect of the shape of the martensite islands on the macroscopic flow behavior. In the second step, the martensite phase was reconstructed from experimental data using a reconstruction procedure based on statistical

correlation functions. In contrast to the CMM, these models incorporate the martensite morphology of the real material and are denoted as statistically equivalent microstructure models (SMM).

In addition, we used two different strategies to model the ferrite phase. A homogeneous ferrite matrix was modeled using an isotropic J2 plasticity model. In contrast to this simple approach, a more advanced modeling strategy was applied that considers the grain structure of the ferrite matrix and uses a crystal plasticity model to describe the constitutive behavior. This strategy takes the crystallographic texture into account when predicting effective material properties like r -values. In the following, the microstructure models are labeled according to the constitutive model used for the ferrite matrix by adding the suffix "-J2" and "-CP", respectively.

3.1. Statistical correlation functions and reconstruction procedure

[32, 33] presented a simple and flexible method based on statistical correlation functions to reconstruct a statistically equivalent model of a given microstructure. They used a combination of the two-point probability function S_2 and the lineal-path function L to achieve good results for the reconstruction process of two-dimensional and three-dimensional microstructures. [36] showed that two-dimensional microstructure models that are statistically equivalent with respect to the S_2 and L functions result in almost identical effective stress-strain curves when used in numerical tensile tests. Thus, the combination of S_2 and L seems to be a good choice as microstructural descriptors for the problem of calculating the effective mechanical response for a heterogeneous two-phase microstructure. According to [37], the two functions are defined in the following way. If a vector \mathbf{r} with length $r = |\mathbf{r}|$ is

randomly placed into a multi-phase sample, the two-point probability function $S_2^{(k)}(\mathbf{r})$ is the probability of having both end points of \mathbf{r} inside phase k . The lineal-path function $L^{(k)}(\mathbf{r})$ is the probability of finding the whole line segment inside phase k . For statistically homogeneous materials, both functions are independent of the absolute position of \mathbf{r} in the microstructure domain. However, both functions depend on the orientation of \mathbf{r} in the case of statistical anisotropy.

The morphological information provided by the evaluation of the S_2 and L functions for a given microstructure are taken as the target for the reconstruction process. For the DP600 considered in this work, the functions characterize the martensite phase and therefore the superscript k is dropped. The reconstructed system is initialized using an artificial distribution of the martensite phase with the same volume content as the real material. The difference between the statistical information of the two systems with respect to an arbitrary correlation function is measured by the mean square error between the corresponding function evaluated for the reconstructed system $(\cdot)^r$ and the target system $(\cdot)^0$. For the three-dimensional reconstruction process, the combination of S_2 and L evaluated in RD, TD and ND was used so that the error has the specific form

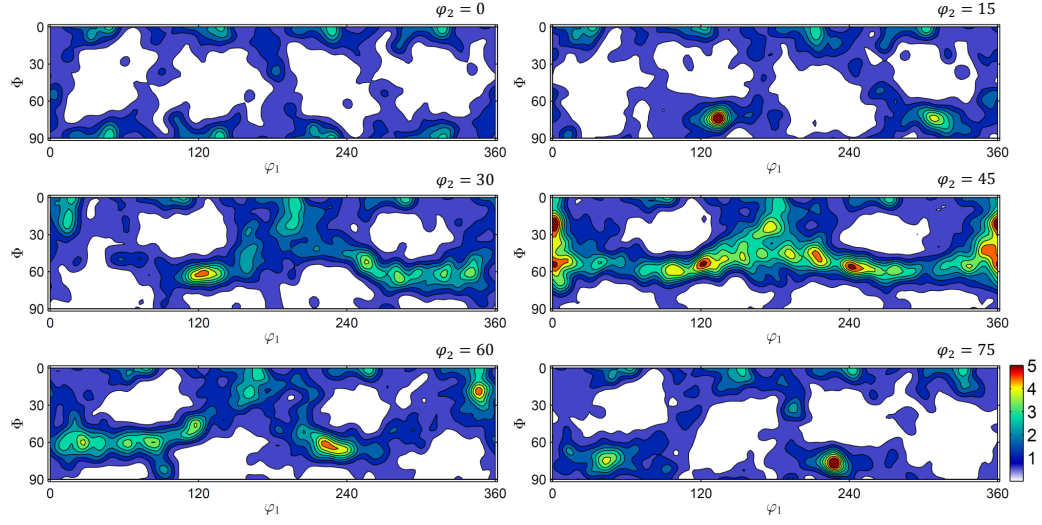
$$\begin{aligned}
E = \sum_{i=0}^n & \left[\left(S_{2,\text{RD}}^r(l_i) - S_{2,\text{RD}}^0(l_i) \right)^2 + \left(S_{2,\text{TD}}^r(l_i) - S_{2,\text{TD}}^0(l_i) \right)^2 \right. \\
& + \left(S_{2,\text{ND}}^r(l_i) - S_{2,\text{ND}}^0(l_i) \right)^2 + \left(L_{\text{RD}}^r(l_i) - L_{\text{RD}}^0(l_i) \right)^2 \\
& \left. + \left(L_{\text{TD}}^r(l_i) - L_{\text{TD}}^0(l_i) \right)^2 + \left(L_{\text{ND}}^r(l_i) - L_{\text{ND}}^0(l_i) \right)^2 \right]. \quad (3)
\end{aligned}$$

Here, l_i is the distance between two points on a line in the corresponding

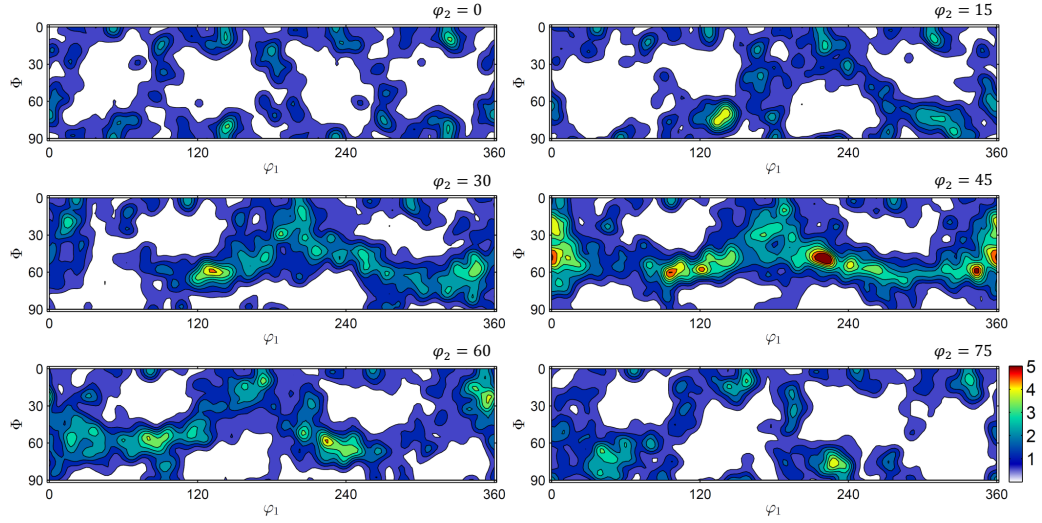
direction measured as the number of pixels (2D) or voxels (3D) depending on the dimensionality of the microstructure representation and n is the size of the analyzed domain. By referring to the physical size of one pixel or voxel, the functions can be compared between microstructure representations with different resolutions. In each iteration of the reconstruction process, the positions of two randomly chosen voxels of opposite phases are swapped and the correlation functions for the reconstructed system are re-evaluated. If this step reduces the error E , the change in the microstructure is accepted. Otherwise, it is refused and two other voxels are swapped.

3.2. Concept microstructure models (CMM)

The CMM were generated to analyze martensite morphologies with clearly distinguishable characteristics. The DREAM.3D software package [38] was used to build the finite element models of the microstructure that represent a volume of $(50\text{ }\mu\text{m})^3$ and were meshed with 100^3 brick elements with reduced integration (C3D8R). First, the grain structure of the ferrite matrix was generated based on the ferrite grain size obtained from the EBSD measurements. The resulting ferrite matrix consists of 3500 grains that were used to represent the crystallographic texture of the material. For that, the ODF obtained from the EBSD data shown in Fig. 3 was reduced to a set of 3500 individual orientations following the procedure described in [39]. From this set, each orientation was assigned to one ferrite grain. Fig. 5 shows the comparison between the ODF obtained from the experimental data and the initial finite element model of the ferrite matrix. The texture is dominated by components belonging to the α - and γ -fiber which is well represented by the microstructure model.



(a)



(b)

Figure 5: Comparison of ODF obtained from (a) the experimental data and (b) the initial finite element model of the ferrite matrix consisting of 3500 grains.

In the second step, the martensite phase was included. For all CMM, a uniform distribution of martensite particles with a volume content of $V^{(m)} = 12\%$ was generated. Using the DREAM.3D features, different aspect ratios were assigned to the martensite islands to create three different martensite morphologies that are denoted as CMM-1 (spherical martensite particles), CMM-2 (martensite particles elongated in rolling direction) and CMM-3 (martensite particles flattened in sheet normal direction). The martensite islands were then inserted into the previously created ferrite matrix. The superposition of the martensite phase with the ferrite matrix caused a reduction of the number of individual orientations in the finite element model by 12%. Since the orientations were deleted rather randomly, the overall texture was almost unaffected. Using this procedure, the underlying ferrite structure is almost the same for all microstructure models which increases the comparability of the simulation results. In addition, each distribution of martensite particles was merged with a homogeneous ferrite matrix. The resulting microstructure models are shown in Fig. 6.

The microstructural correlation functions described in Section 3.1 were used to characterize the different martensite morphologies. Fig. 7 shows the two-point probability function S_2 and the lineal-path function L evaluated in RD, TD and ND for CMM-1, CMM-2 and CMM-3. For CMM-1, both functions give the same results for all directions except for a small deviation of S_2 evaluated in RD. Thus, the distribution of martensite particles belonging to CMM-1 is statistically isotropic. In contrast, the results of S_2 and L depend on the direction when evaluated for CMM-2 and CMM-3. The martensite phase of these models is statistically anisotropic.

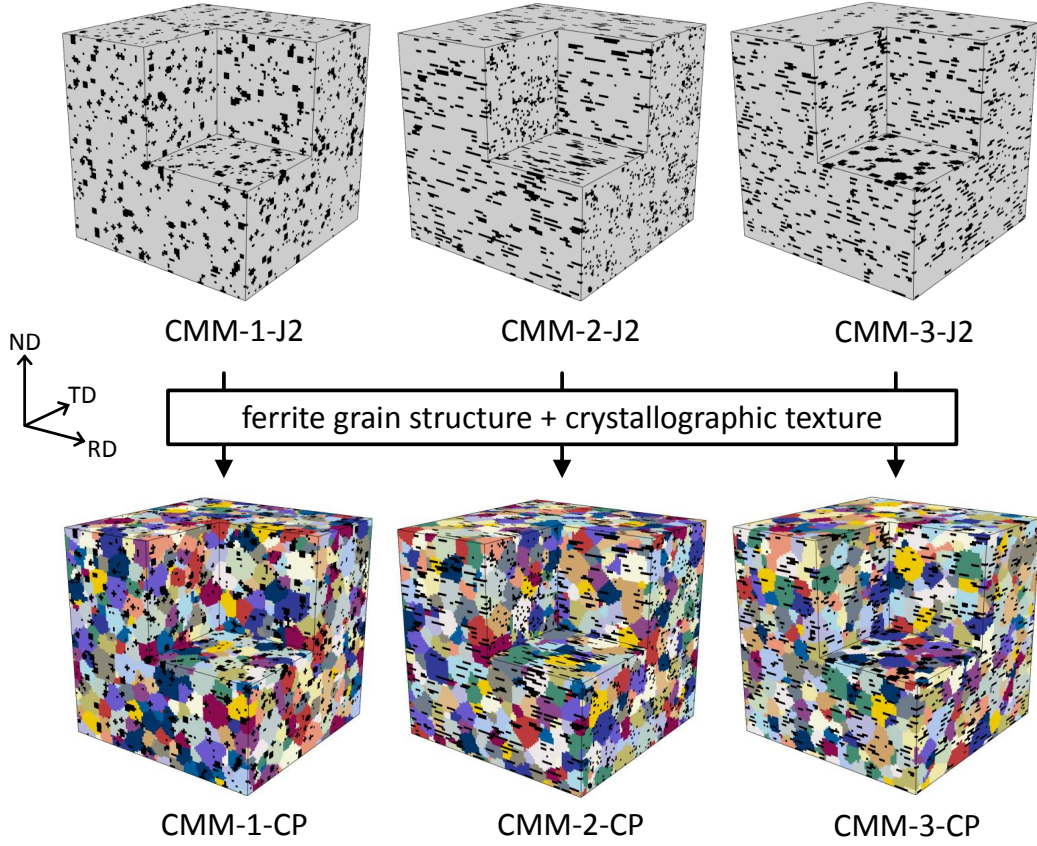
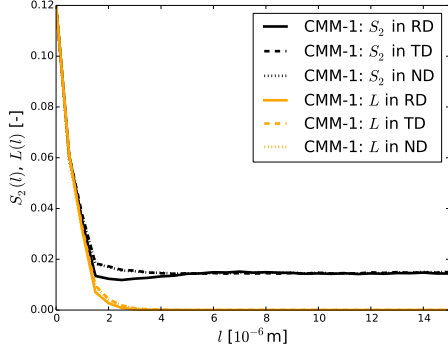
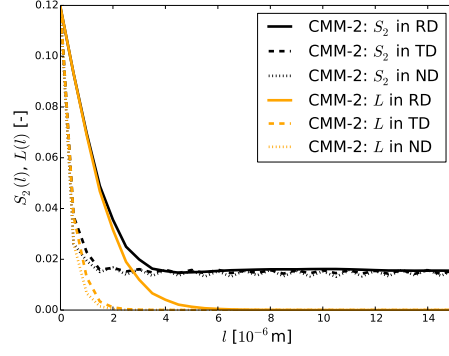


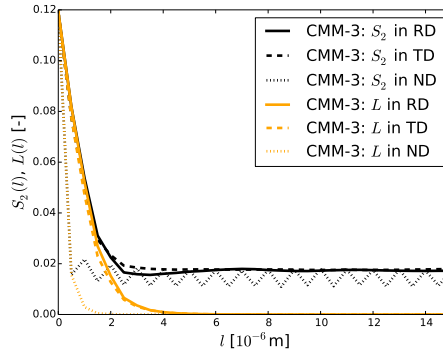
Figure 6: Concept microstructure models (CMM) with a martensite content of $V^{(m)} = 12\%$ and distinct martensite morphologies generated using different DREAM.3D settings. Finite element models with a homogeneous matrix neglecting the grain structure of the ferrite phase: CMM-1-J2, CMM-2-J2 and CMM-3-J2. Finite element models using a crystal plasticity model for the ferrite phase to take the crystallographic texture into account: CMM-1-CP, CMM-2-CP and CMM-3-CP (Note that the ferrite grain structure is the same although the coloring of the individual grains is different.).



(a)



(b)



(c)

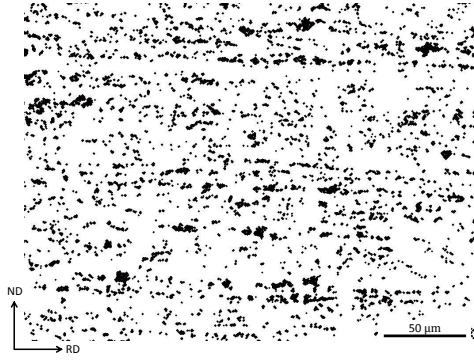
Figure 7: Statistical characterization of the martensite morphology in the concept microstructure models (CMM) using the microstructural correlation functions S_2 and L evaluated in three directions. The results are plotted using the physical length scale (edge length of one element is equal to $0.5 \mu\text{m}$).

3.3. Statistically equivalent microstructure models (SMM)

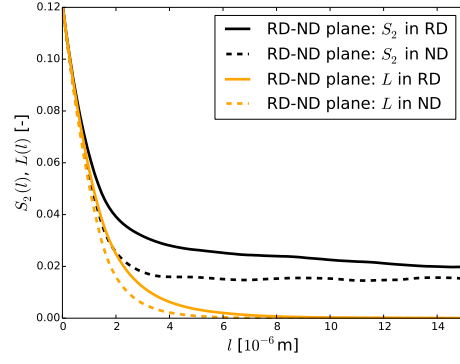
A family of three-dimensional microstructure models with a martensite morphology that is statistically equivalent to the DP600 investigated in this work was generated using the reconstruction method outlined in Section 3.1.

The statistical information required for the reconstruction process were collected from the micrographs shown in Fig. 2. The images were converted to binary images to separate the two phases. Subsequently, a combination of the image processing operations erosion and dilation was used to exclude grain boundaries. The processed images were used to evaluate the microstructural correlation functions and are shown in Fig. 8 (a) and (c). As can be seen from Fig. 8 (b) and (d), S_2 and L depend on the direction in which they are evaluated. The results indicate that the martensite morphology in the real material is statistically anisotropic. Compared to the evaluation in ND, both functions have higher values in RD and TD which reflects the slight martensite banding that can be recognized in Fig. 8 (a).

The statistical information that serve as target values for the reconstruction process were assembled in the following way: S_2 and L in RD and ND were taken from the cross section orthogonal to TD and the information in TD were taken from the cross section orthogonal to RD. Four different but statistically equivalent martensite morphologies that are denoted as SMM-1 to SMM-4 were generated based on the same target values. For each distribution of martensite particles, the reconstruction process was started with an initial martensite configuration similar to that of CMM-1 with a martensite content of $V^{(m)} = 12\%$. Fig. 9 (a) shows the evolution of the S_2 function evaluated in RD for SMM-1 during the reconstruction process. After $5 \cdot 10^6$



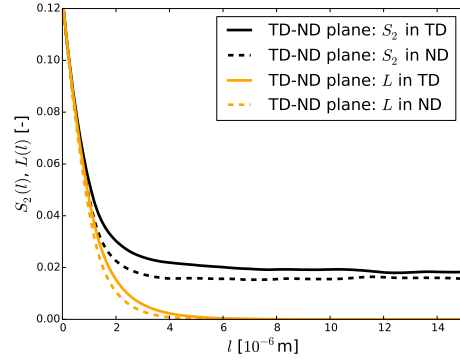
(a)



(b)



(c)



(d)

Figure 8: Statistical characterization of the martensite phase in DP600. Binarized and processed micrographs and evaluation of microstructural correlation functions for cross sections orthogonal to TD, (a) and (b), and orthogonal to RD, (c) and (d).

iterations, the reconstructed martensite phase exhibits the same statistical characteristics as the real material. The same holds true for the remaining functions used in the reconstruction process as shown in Fig. 9 (b).

Again, two different modeling approaches for the ferrite phase were applied. The four statistically equivalent martensite morphologies were combined with a homogeneous matrix and with the ferrite grain structure described in Section 3.2. Like the CMM, the finite element models were meshed with 100^3 elements of type C3D8R using an element edge length of $0.5\text{ }\mu\text{m}$. Fig. 10 shows the resulting microstructure models.

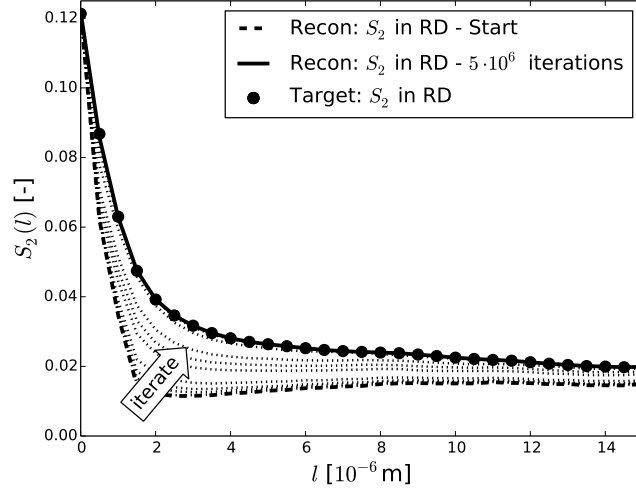
4. Simulation approach

4.1. Constitutive modeling of martensite

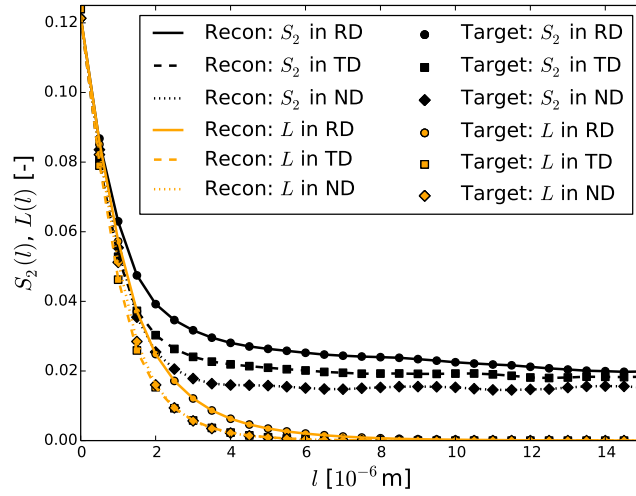
The plastic flow behavior of the martensite phase was approximated using an isotropic plasticity model as implemented in Abaqus/Standard [40]. Following [41], the flow stress is expressed as a function of strain according to

$$\sigma_f = \sigma_0 + \alpha M \mu \sqrt{b} \sqrt{\frac{1 - \exp(-M k_2 \varepsilon_p)}{k_2 L}}. \quad (4)$$

This approach has been used for full-field simulations of dual-phase steels by various authors [7, 3, 42]. The first term in Eq. (4) defines the yield stress and is given as



(a)



(b)

Figure 9: Statistical characterization of martensite phase in SMM-1. (a) Evolution of S_2 evaluated in RD during the reconstruction process. (b) Comparison of statistical information between SMM-1 and target values after $5 \cdot 10^6$ iterations.

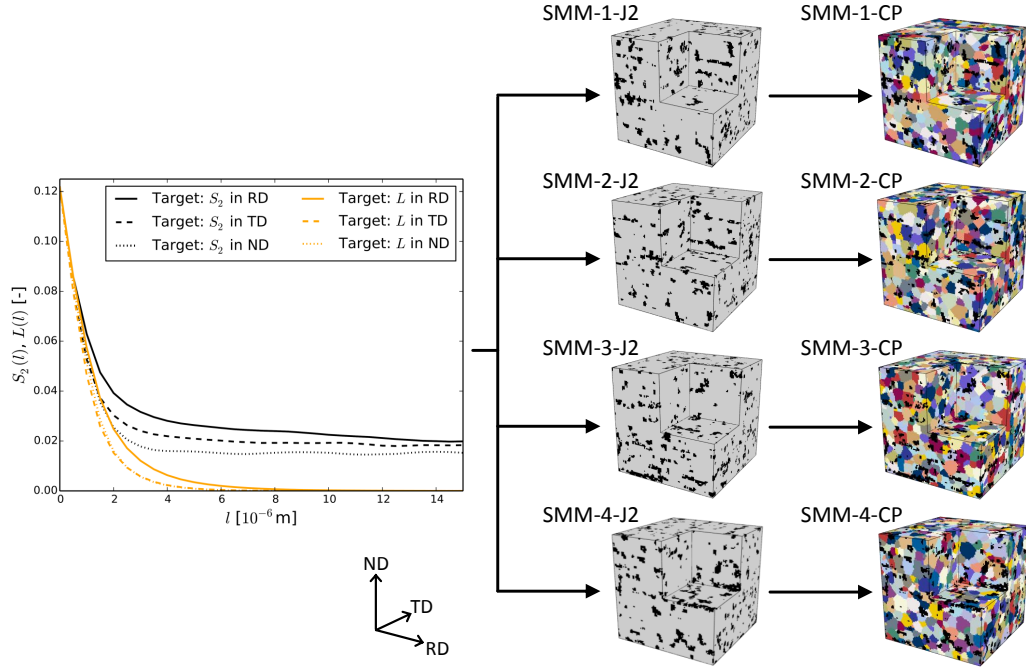


Figure 10: Family of statistically equivalent microstructure models (SMM) reconstructed from the same set of statistical information that represents the martensite morphology of the DP600. Two different approaches to model the ferrite matrix are shown (Note that the grain structure is the same although the coloring of the individual grains is different.).

$$\begin{aligned}
\sigma_0 = & 77 \text{ MPa} + 80 \text{ MPa} \cdot (\% \text{Mn}) + 750 \text{ MPa} \cdot (\% \text{P}) + 60 \text{ MPa} \cdot (\% \text{Si}) \\
& + 80 \text{ MPa} \cdot (\% \text{Cu}) + 45 \text{ MPa} \cdot (\% \text{Ni}) + 60 \text{ MPa} \cdot (\% \text{Cr}) \\
& + 11 \text{ MPa} \cdot (\% \text{Mo}) + 5000 \text{ MPa} \cdot (\% \text{N}_{\text{ss}}) \\
& + 3065 \text{ MPa} \cdot (\% \text{C}_{\text{ss}}^{(\text{m})}) - 161 \text{ MPa}.
\end{aligned} \tag{5}$$

Except for the carbon concentration, the global chemical composition of the dual-phase steel given in Table 1 was used to evaluate Eq. (5). The carbon concentration in martensite has a significant effect on its strength and was estimated as $C_{\text{ss}}^{(\text{m})} = 0.61 \%$ from the rule of mixture according to

$$C^{(\text{m})} = C^{(\text{f})} + \frac{C^{(\text{DP})} - C^{(\text{f})}}{V^{(\text{m})}}. \tag{6}$$

For this approximation, $C^{(\text{f})} = 0.022 \%$ was taken as the maximum carbon content in ferrite [29, 43, 15]. The second term in Eq. (4) represents the strain hardening. The parameters are $M = 3.0$ (Taylor factor), $\alpha = 0.33$ (a constant), $\mu = 80000 \text{ MPa}$ (shear modulus), $b = 2.5 \cdot 10^{-10} \text{ m}$ (Burger's vector), $L = 3.8 \cdot 10^{-8} \text{ m}$ (mean free path), $k_2 = 40$ (recovery rate) and were taken from [41].

4.2. Constitutive modeling of ferrite

As described in Section 3, two different approaches were applied to model the ferrite matrix. The microstructure models labeled with the suffix "-J2" neglect the grain structure of the ferrite phase and an isotropic J2 plasticity model was used to define the material behavior. The flow stress was given as a function of the plastic strain according to

$$\sigma_f = \sigma_0 + \theta_\infty \varepsilon_p + (\sigma_\infty - \sigma_0) \left(1 - \exp \left(-\frac{\theta_0 - \theta_\infty}{\sigma_\infty - \sigma_0} \varepsilon_p \right) \right). \quad (7)$$

Here, the parameters σ_0 , σ_∞ , θ_0 and θ_∞ define the strain hardening. A Young's modulus of $E = 210$ GPa and a Poisson's ratio of $\nu = 0.3$ were taken as elastic constants. The model given in Eq. (7) was implemented using the UHARD interface of Abaqus/Standard.

The suffix "-CP" denotes microstructure models that consider the crystallographic texture of the material by incorporating the grain structure of the ferrite matrix. A crystal plasticity model was applied to define the constitutive behavior and to account for individual grain orientations. The material model is briefly described in the following and was implemented as a UMAT subroutine for Abaqus/Standard according to the scheme presented by [44]. Using the decomposition of the deformation gradient $\mathbf{F} = \mathbf{F}_e \mathbf{F}_p$, the plastic velocity gradient in the intermediate configuration is defined as the sum of shear rates on all slip systems according to

$$\mathbf{L}_p = \dot{\mathbf{F}}_p \mathbf{F}_p^{-1} = \sum_{\alpha=1}^n \dot{\gamma}^\alpha \mathbf{m}^\alpha \otimes \mathbf{n}^\alpha. \quad (8)$$

Here, \mathbf{m}^α and \mathbf{n}^α denote the slip direction and the normal to the slip plane for each slip system. For the body-centered cubic crystal structure of the ferrite phase, slip systems of type $\{110\} \langle 111 \rangle$ and $\{112\} \langle 111 \rangle$ were considered, i.e. $n = 24$. The shear rate $\dot{\gamma}^\alpha$ is given by the power law

$$\dot{\gamma}^\alpha = \dot{\gamma}_0 \left| \frac{\tau^\alpha}{g^\alpha} \right|^{1/m} \text{sign}(\tau^\alpha), \quad (9)$$

which is a function of the resolved shear stress τ^α and a hardening variable g^α . A reference shear rate of $\dot{\gamma}_0 = 0.001 \text{ s}^{-1}$ and a rate sensitivity parameter

$m = 0.0125$ were chosen to define a low strain rate dependence. The resolved shear stress follows from $\tau^\alpha = (\mathbf{C}_e \mathbf{S}) : (\mathbf{m}^\alpha \otimes \mathbf{n}^\alpha)$ with $\mathbf{C}_e = \mathbf{F}_e^T \mathbf{F}_e$ by using the stress tensor $\mathbf{S} = \frac{1}{2} \mathbb{C} : (\mathbf{F}_e^T \mathbf{F}_e - \mathbf{I})$ in the intermediate configuration. The elastic constants $C_{11} = 226$ GPa, $C_{12} = 140$ GPa and $C_{44} = 116$ GPa of pure iron were used [45]. The evolution of the slip resistance g^α is given by

$$\dot{g}^\alpha = \frac{d\hat{\tau}}{d\Gamma} \sum_{\beta=1}^n q^{\alpha\beta} |\dot{\gamma}^\beta| \quad (10)$$

with

$$\hat{\tau}(\Gamma) = \tau_0 + (\tau_1 + \Theta_1 \Gamma) \left[1 - \exp\left(-\frac{\Theta_0 \Gamma}{\tau_1}\right) \right]. \quad (11)$$

Self and latent hardening effects are taken into account by the interaction matrix $q^{\alpha\beta}$ in Eq. (10). A value of 1.0 was assigned to the diagonal elements ($\alpha = \beta$). The latent to self hardening ratio is represented by the off-diagonal elements ($\alpha \neq \beta$) which were set to 1.4 without further distinguishing between slip systems. The parameters τ_0 , τ_1 , Θ_0 and Θ_1 define the hardening behavior depending on the accumulated plastic shear calculated from

$$\Gamma = \int_0^t \sum_{\alpha=1}^n |\dot{\gamma}^\alpha| dt. \quad (12)$$

4.3. Simulation setup and homogenization procedure

The finite element models presented in Section 3 were used to calculate the micromechanical stress and strain fields for different loading conditions. The simulations were performed using periodic boundary conditions described by

$$\mathbf{u}^b - \mathbf{u}^a = \bar{\mathbf{F}}(\mathbf{X}^b - \mathbf{X}^a) - (\mathbf{X}^b - \mathbf{X}^a), \quad (13)$$

i.e. the displacements \mathbf{u}^a and \mathbf{u}^b of two equivalent points \mathbf{X}^a and \mathbf{X}^b located on opposite surfaces in the undeformed configuration are coupled by the macroscopic deformation gradient $\bar{\mathbf{F}}$. Following [46], the components of the displacement gradient $\bar{\mathbf{H}}$ were represented by the displacements of three auxiliary nodes that were used to constrain the displacements of the surface nodes. The components of the macroscopic deformation gradient $\bar{\mathbf{F}} = \bar{\mathbf{H}} + \mathbf{1}$ and the macroscopic first Piola-Kirchhoff stress $\bar{\mathbf{P}}$ were derived from the displacements and reaction forces of these control nodes. Other stress and strain measures can be calculated from these quantities and the simulation results could be processed in the same way as the experimental data. For example, the effective true stress $\bar{\sigma}$ and true strain $\bar{\epsilon}$ are calculated according to

$$\bar{\sigma} = \frac{1}{\det \bar{\mathbf{F}}} \bar{\mathbf{P}} \bar{\mathbf{F}}^T, \quad (14)$$

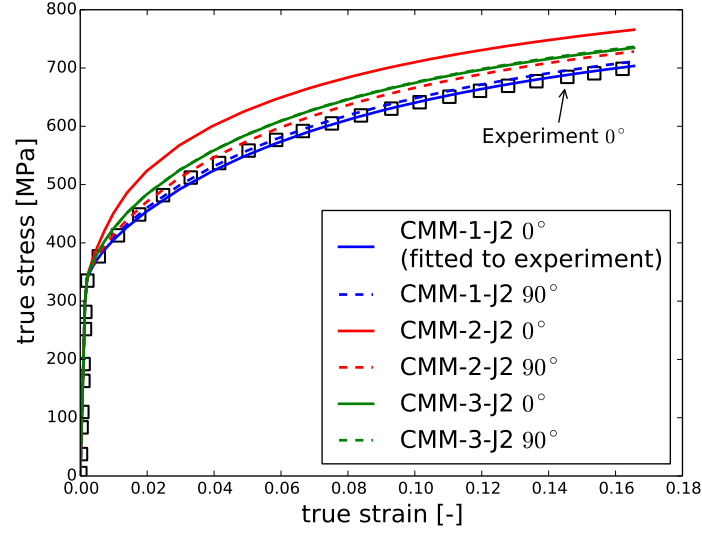
$$\bar{\epsilon} = \ln(\bar{V}) = \ln\left(\sqrt{\bar{\mathbf{F}} \bar{\mathbf{F}}^T}\right). \quad (15)$$

5. Results and discussion

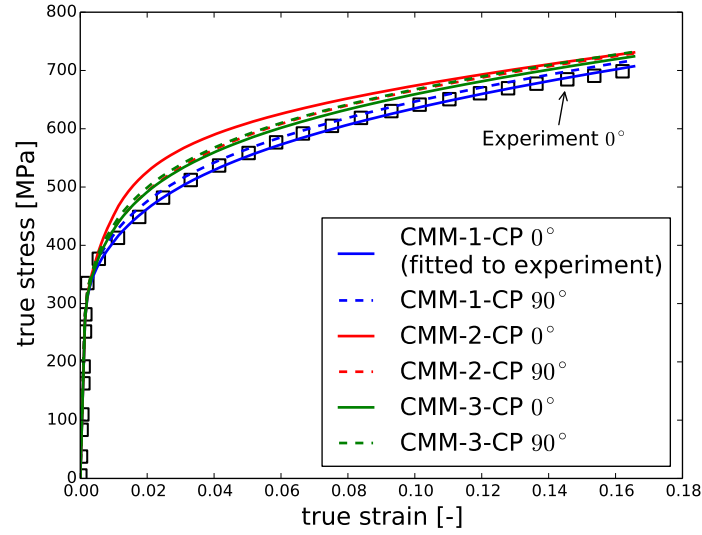
5.1. Numerical study: Flow behavior of concept microstructure models

Numerical tensile tests in RD (0°) and TD (90°) were performed for all concept microstructure models. While the hardening behavior of the martensite phase was prescribed by Eqs. (4) and (5) and the parameters given in Section 4.1, the hardening parameters of the ferrite phase were determined by fitting the effective stress-strain curve from a numerical tensile test in RD to the experimental data. The following hardening parameters were

obtained by using the microstructure models CMM-1-J2 and CMM-1-CP with spherical martensite particles for the fitting procedure: $\sigma_0 = 330$ MPa, $\sigma_\infty = 550$ MPa, $\theta_0 = 2080$ MPa and $\theta_\infty = 155$ MPa to define the hardening according to Eq. (7) for the isotropic J2 plasticity model and $\tau_0 = 128$ MPa, $\tau_1 = 145$ MPa, $\Theta_0 = 78$ MPa and $\Theta_1 = 21$ MPa to define the hardening according to Eq. (11) for the crystal plasticity model. The effective stress-strain curves of CMM-1-J2 and CMM-1-CP that were fitted to the experimental results are shown in Fig. 11 (a) and (b). Both microstructure models are able to reproduce the strain hardening behavior of the DP600 in rolling direction. The additional results shown in Fig. 11 were obtained with the same sets of parameters depending on the constitutive model used for the ferrite matrix. Fig. 12 shows the evolution of the plastic strain ratio for the different modeling approaches. In addition, the simulation results were processed in the same way as the experimental data to determine the r-values for tensile strains between 5 % and 15 %. Table 3 summarizes the comparison between the results of the numerical tensile tests using the concept microstructure models. The simulation results indicate that the morphology of the martensite phase affects the hardening behavior and the r-values of a dual-phase steel. However, the homogenized results were different depending on whether or not the crystallographic texture was considered in the microstructure representation. For models with a homogeneous ferrite matrix, the shape of the homogeneously distributed martensite particles is the only microstructural feature that affects the macroscopic behavior. In this case, the predicted effective response can be deduced from the statistics of the martensite morphologies shown in Fig. 7. The spherical martensite particles of CMM-1-J2

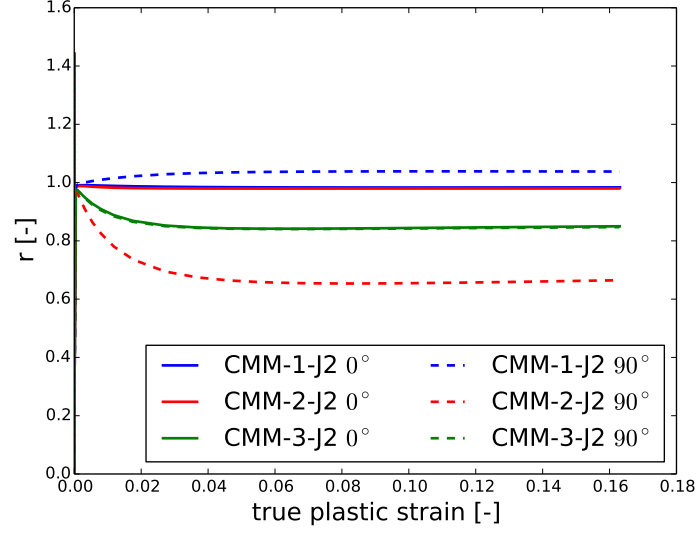


(a)

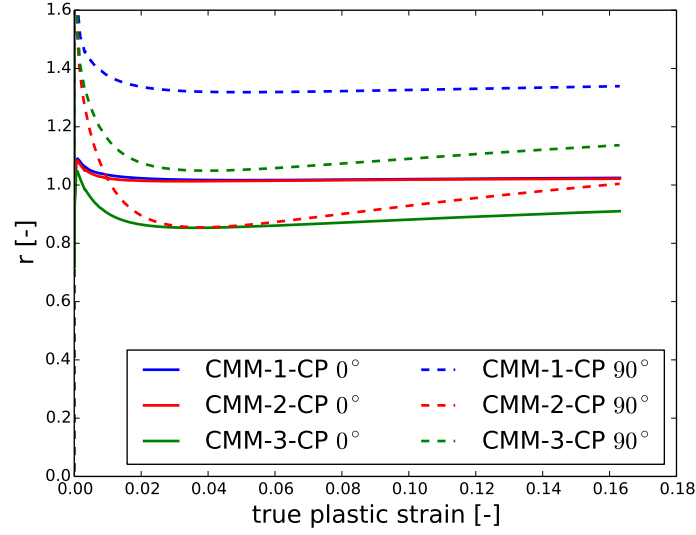


(b)

Figure 11: Stress-strain curves from numerical tensile tests in RD (0°) and TD (90°) for the CMM using (a) the isotropic J2 plasticity model and (b) the crystal plasticity model for the ferrite matrix (experimental data taken from [35]).



(a)



(b)

Figure 12: Evolution of plastic strain ratio for numerical tensile tests in RD (0°) and TD (90°) for the CMM using (a) the isotropic J2 plasticity model and (b) the crystal plasticity model for the ferrite matrix.

Table 3: Comparison of effective mechanical response of DP microstructure as predicted by different concept microstructure models for numerical tensile tests in RD (0°) and TD (90°).

Model	Microstructural features	Stress-strain	$r_{0/5-15}$	$r_{90/5-15}$
CMM-1-J2	spherical martensite, no texture	\approx isotropic	0.98	1.04
CMM-2-J2	elongated martensite, no texture	stronger in 0°	0.98	0.66
CMM-3-J2	flattened martensite, no texture	\approx isotropic	0.85	0.84
CMM-1-CP	spherical martensite, texture	stronger in 90°	1.02	1.33
CMM-2-CP	elongated martensite, texture	stronger in 0°	1.02	0.95
CMM-3-CP	flattened martensite, texture	\approx isotropic	0.89	1.10

lead to nearly identical stress-strain curves for tensile tests in 0° and 90° and $r_0 \approx r_{90} \approx 1$. The small differences between the effective behavior in the two directions is most likely a consequence of the fact that the martensite morphology of CMM-1 is not perfectly isotropic, which is indicated by the slight deviation of S_2 when evaluated in RD for the corresponding finite element model (cf. Fig. 7 (a)). In contrast, the martensite morphologies of CMM-2-J2 and CMM-3-J2 are statistically anisotropic. The fibrous martensite particles in CMM-2-J2 are elongated in RD which results in higher values for S_2 and L in that direction and introduces an anisotropic hardening behavior. This structure increases the strength for tensile tests in RD which is in agreement with the findings of [47] and can be related to a better stress transfer as supposed by [48]. For CMM-2-J2, $r_{90} < 1$ is a consequence of the fibrous martensite aligned with RD that impedes the plastic flow in RD compared to ND. At the same time, $r_0 \approx 1$ follows directly from the statistically isotropic

martensite morphology with respect to the TD-ND plane. The stress-strain curves predicted by CMM-3-J2 are identical in both directions and $r_0 \approx r_{90}$. This follows from the statistically isotropic martensite morphology in the RD-TD plane in which the numerical tensile tests were performed. Since the flattened shape of the martensite particles facilitates plastic flow in ND compared to strains in the RD-TD plane, the r-values are smaller than 1. The simulation results are different if the crystallographic texture is considered as an additional microstructural feature. Regarding the stress-strain curves, both modeling approaches exhibit the same tendency with respect to the effect of the martensite morphology. However, the differences between the stress-strain curves for microstructure models with different martensite morphologies become smaller at high strains if the ferrite matrix is modeled using the crystal plasticity approach. At the same time, the incorporation of the crystallographic texture changes the degree of anisotropy of the predicted r-values. While anisotropy is introduced for CMM-1 and CMM-3, the degree of anisotropy becomes smaller for CMM-2. In contrast to the J2 simulations, the plastic strain ratios are not necessarily constant for high tensile strains. This can be seen for r_{90} of CMM-2-CP and CMM-3-CP shown in Fig. 12 (b). It can be concluded that both the martensite morphology and the crystallographic texture of the material influence the effective material behavior and can contribute to anisotropic mechanical properties of the DP structure. Fig. 13 shows the spatially resolved von Mises stress field in the ferrite matrix for CMM-1-J2 and CMM-1-CP used in the fitting procedure. Although both finite element models contain the same martensite morphology and were fitted to the same macroscopic stress-strain curve, the local stress fields differ

significantly. The two-phase microstructure causes an inhomogeneous stress distribution for both modeling approaches. However, the level of heterogeneity is much higher if the grain structure of the ferrite matrix is considered. This dependence of the micromechanical fields on the chosen modeling approach has also been shown by [49] and [50]. Since micromechanical damage affects the effective properties of the dual-phase steel, the more detailed representation of the microstructure is crucial if the description of damage and failure is included in the full-field simulations. If the analysis of the local behavior is more important than the prediction of effective properties, a smaller region of the microstructure and a higher resolution in space (i.e. a finer mesh) can be considered. This can be computationally very demanding, especially for three-dimensional simulations.

5.2. Flow behavior of statistically equivalent microstructure models

Numerical tensile tests using the statistically equivalent microstructure models were performed to predict the plastic flow behavior of the DP600 investigated in this work. The hardening parameters of the constitutive models used for the ferrite phase were recalibrated by fitting the effective stress-strain curve of SMM-1-J2 and SMM-1-CP to the experimental tensile test in RD. The adjusted parameters for the J2 plasticity model are $\sigma_0 = 315$ MPa, $\sigma_\infty = 550$ MPa, $\theta_0 = 2030$ MPa and $\theta_\infty = 155$ MPa. For the crystal plasticity model, the recalibration gave $\tau_0 = 128$ MPa, $\tau_1 = 148$ MPa, $\Theta_0 = 107$ MPa and $\Theta_1 = 12$ MPa. As shown in Fig. 14, it is again possible to reproduce the stress-strain curve with both modeling approaches.

The recalibrated parameters were used to simulate tensile tests in RD and TD for all SMM. Regardless of the modeling approach used for the ferrite ma-

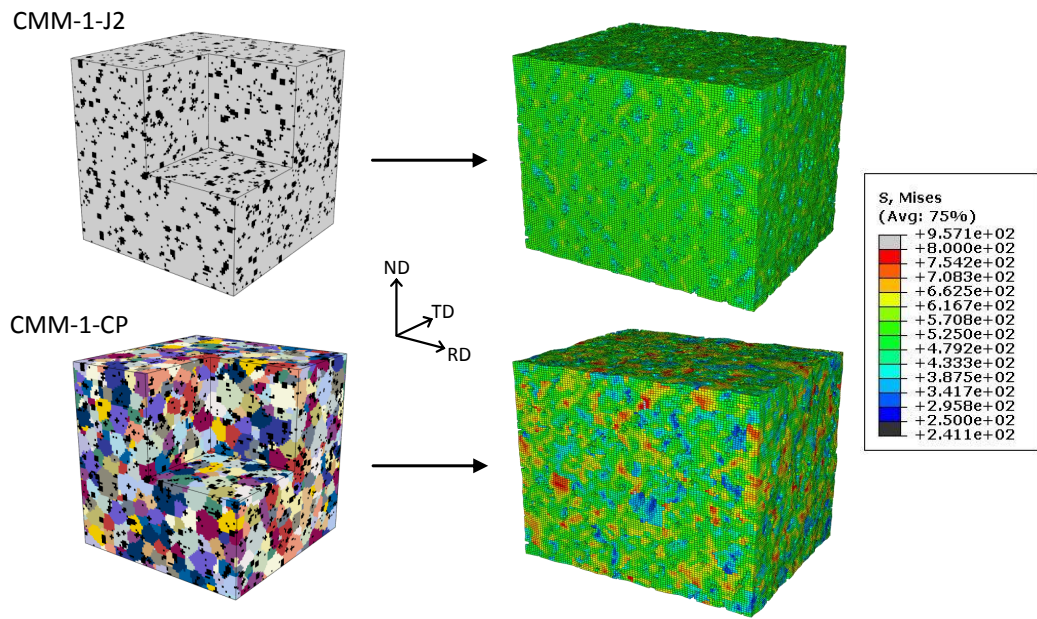
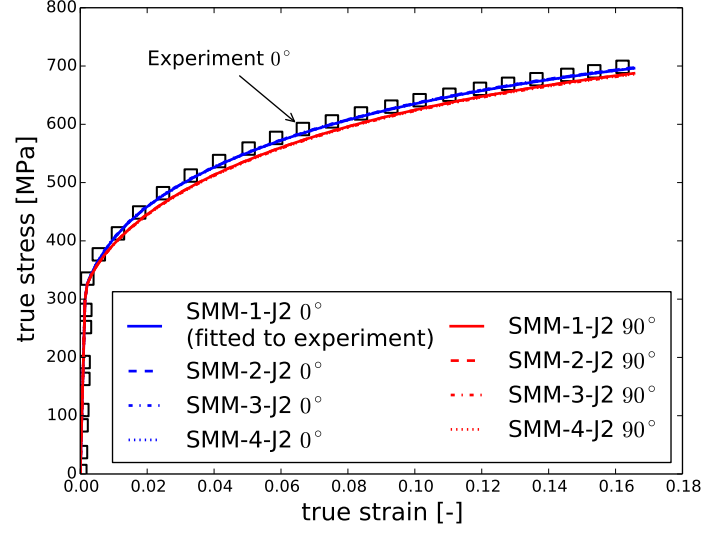
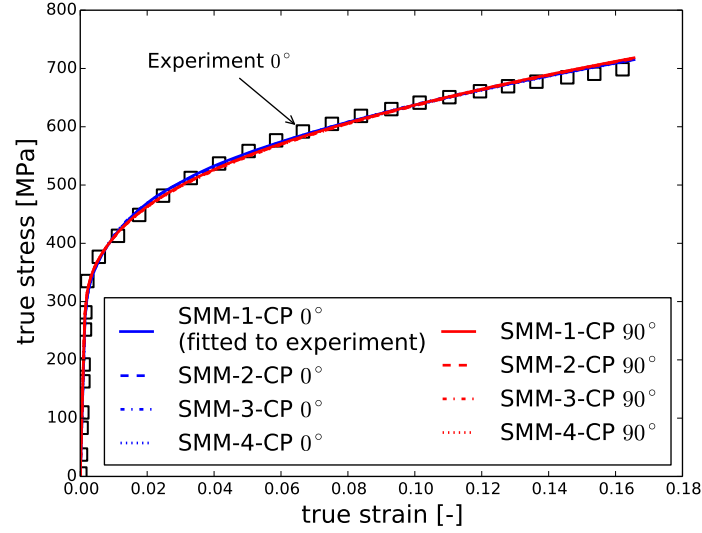


Figure 13: Distribution of von Mises stress in MPa for CMM-1-J2 and CMM-1-CP during the parameter identification for an effective strain of 16.5% in RD. Only elements belonging to the ferrite phase are shown in the deformed mesh.



(a)



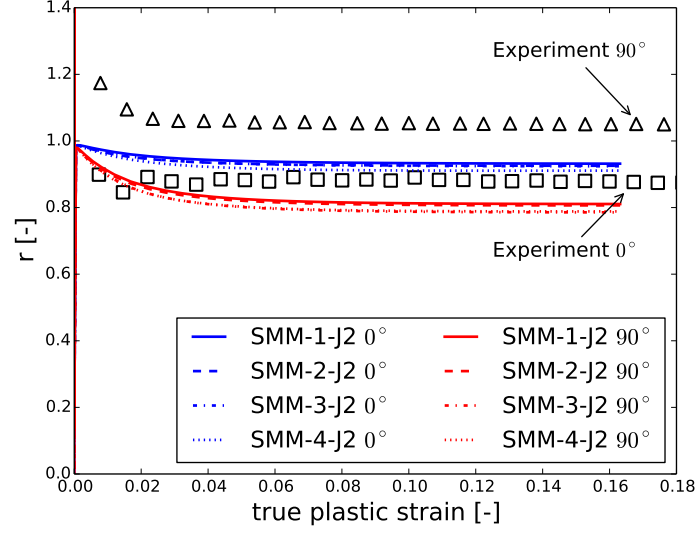
(b)

Figure 14: Stress-strain curves from numerical tensile tests in RD (0°) and TD (90°) for the SMM using (a) the isotropic J2 plasticity model and (b) the crystal plasticity model for the ferrite matrix (experimental data taken from [35]).

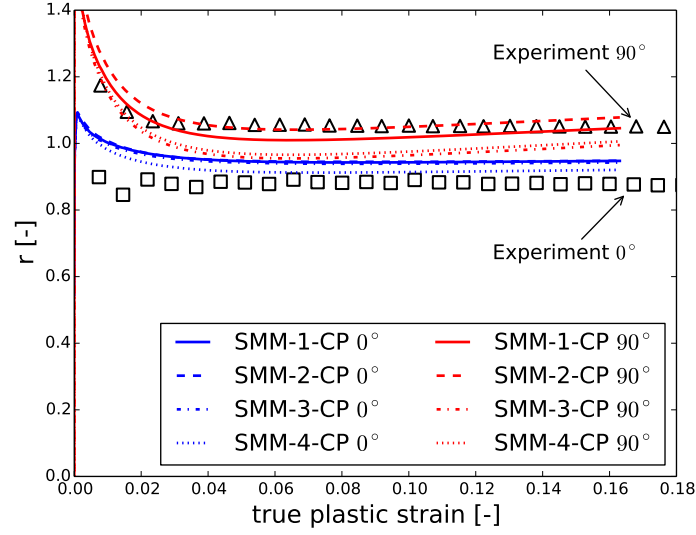
trix, the same effective stress-strain curves were obtained for the four SMM that are identical with respect to the statistics of the martensite morphology and distribution. For simulations with the homogeneous ferrite matrix, the material is slightly stronger when loaded in RD (Fig. 14 (a)). As shown in Fig. 10, the S_2 and L functions have the highest values when evaluated in RD. This corresponds to an elongation of the martensite morphology in this direction and is the reason for higher strength as discussed in the previous section. As shown in Fig. 14 (b), the stress-strain curves are almost identical in both directions when the crystal plasticity model is applied. These results are in better agreement with the isotropic hardening behavior of the DP600. Obviously, the slight anisotropy of the flow curves due to the martensite morphology (Fig. 14 (a)) is compensated by the crystallographic texture in case of the SMM-CP models (Fig. 14 (b)).

Fig. 15 shows the evolution of the plastic strain ratios obtained from experiments and simulations. A comparison between the experimental results and the mechanical response predicted by the SMM is given in Table 4.

The r -values predicted from simulations that use different realizations of the same statistical information are almost identical if a homogeneous ferrite matrix is considered. This extends the findings of [36] on predicting effective material properties from two-dimensional two-phase microstructures that are identical with respect to S_2 and L . The results indicate that the martensite morphology that is statistically equivalent to the real material causes an anisotropic plastic flow behavior. However, while r_0 is close to the experimental value, the simulations predict $r_0 > r_{90}$ which is qualitatively wrong when compared to the experimental data. The finite element models with



(a)



(b)

Figure 15: Evolution of plastic strain ratio for numerical tensile tests in RD (0°) and TD (90°) for the SMM using (a) the isotropic J2 plasticity model and (b) the crystal plasticity model for the ferrite matrix (experimental data taken from [35]).

Table 4: Comparison between experimental results and effective mechanical response predicted by statistically equivalent microstructure models.

Model	Microstructural features	Stress-strain	$r_{0/5-15}$	$r_{90/5-15}$
Experiment	Real material	Isotropic	0.88	1.05
SMM-1-J2	Stat. equivalent	Stronger in 0°	0.93	0.81
SMM-2-J2	martensite		0.93	0.81
SMM-3-J2	morphology,		0.93	0.79
SMM-4-J2	no texture		0.91	0.79
SMM-1-CP	Stat. equivalent	Isotropic	0.94	1.03
SMM-2-CP	martensite		0.95	1.06
SMM-3-CP	morphology,		0.94	0.97
SMM-4-CP	texture		0.92	0.98

the crystal plasticity model for the ferrite matrix incorporate the crystallographic texture of the DP600 and a statistically equivalent morphology of the martensite phase. Some scatter is observed for the prediction of r_{90} from these models. This is a consequence of the procedure performed to generate the finite element models. The different distributions of martensite particles remove different parts of the same underlying ferrite grain structure that carries the orientation information. Although the ODF evaluated for these models were almost identical, the effective r-values are still affected by this procedure. This shows the high sensitivity of the simulation results to the representation of the crystallographic texture. Nevertheless, the predicted r-values are qualitatively correct for all four models (SMM-1-CP to SMM-4-CP), i.e. $r_0 < r_{90}$, and are close to the experimental values. Although

the incorporation of the crystallographic texture increases the modeling effort and the computation time of the full-field simulations, it is necessary to consider this microstructural feature in order to improve the prediction of the plastic anisotropy. On the other hand, a realistic martensite morphology has to be considered as well. This can be seen when the simulation results of CMM-1-CP shown in the previous section are compared with the experimental data. This model takes the crystallographic texture into account but neglects the statistically anisotropic morphology of the martensite phase which results in an anisotropic hardening behavior and an overprediction of the r -values. The latter was also found by [28] when predicting the r -values of a DP using a visco-plastic self-consistent (VPSC) polycrystal model that ignores any effect of the martensite phase on the macroscopic properties.

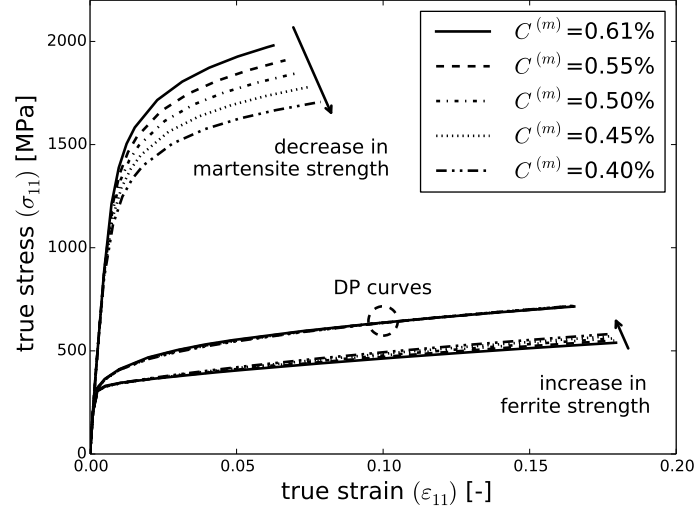
For the applied loading conditions, the more advanced modeling strategy allows for a good representation of the DP600 behavior. However, the difference between r_0 and r_{90} , i.e. the degree of planar anisotropy, is still too small. In this work, all microstructure information used for the generation of the finite element models were obtained from sections in the middle of the sheet. Thus, gradients through the sheet thickness regarding the martensite morphology or the crystallographic texture that may affect the macroscopic properties were not considered. Furthermore, not all micromechanical mechanisms that are known to affect the properties of dual-phase steels are included in the modeling approach. However, microstructural features like an initial distribution of residual stresses and an inhomogeneous hardening of the ferrite matrix are considered to be of minor importance compared to the effect of the martensite morphology and the crystallographic texture. To further

improve the predictive capabilities of the virtual testing approach, in particular for non-monotonic loading paths and the prediction of the well-known Bauschinger effect, it may be necessary to consider additional mechanisms. As discussed in the next section, the rough approximation of the mechanical phase contrast might be another reason for the deviation from the experimental results.

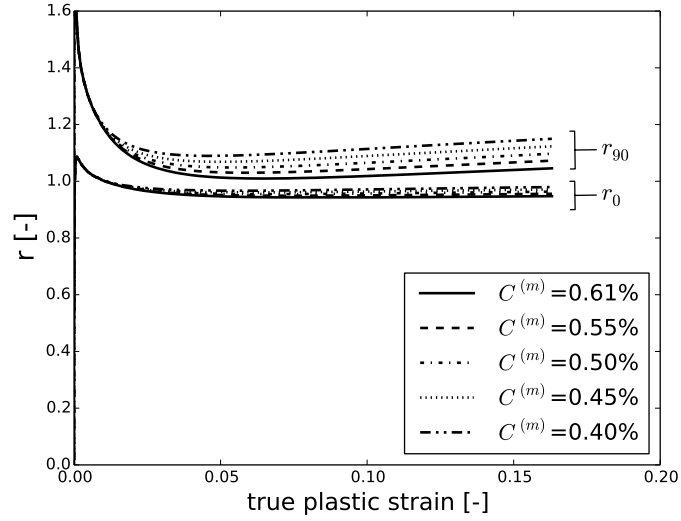
5.3. Effect of mechanical phase contrast on plastic strain ratios

Additional simulations with SMM-1-CP were performed to assess the effect of the mechanical phase contrast on the predicted r-values. The mechanical phase contrast depends on the chemical composition of the material and on the processing history. For example, a tempering process is known to decrease the difference in strength between the two phases of a DP structure [51, 52, 53]. In this work, the flow behavior of the martensite phase was approximated using the empirical model given by Eqs. (4) and (5). Although often used in the literature, this approach can only give a rough estimate of the yield stress and strength of the martensite particles. The martensite strength was changed systematically by varying the carbon content used in Eq. (5). The carbon content was reduced stepwise from its approximated value of $C^{(m)} = 0.61\%$ to $C^{(m)} = 0.55\%$, $C^{(m)} = 0.50\%$, $C^{(m)} = 0.45\%$ and $C^{(m)} = 0.40\%$ to decrease the strength of the martensite particles. Hence, different mechanical properties were assigned to the martensite phase without changing its volume content, morphology and distribution. At the same time, the ferrite parameters were recalibrated by fitting the effective stress-strain curve of SMM-1-CP to the experimental data. Fig. 16 (a) shows how the partitioning of the stress and strain components in tensile direction

is changed when the mechanical phase contrast is decreased while keeping the effective strength of the dual-phase structure constant. In contrast to the homogenization procedure described in Section 4, the stress and strain tensors of the individual phases were obtained from the phase-specific volume averages of the Cauchy stress field and the true strain field, respectively. As shown in Fig. 16 (b), the variation of the mechanical phase contrast affects the predicted r-values. Since a smaller difference in strength between the two phases leads to a less pronounced influence of the martensite morphology on the effective properties of the DP structure, the anisotropic material response becomes dominated by the crystallographic texture. In the present case, a low mechanical phase contrast leads to higher r-values for tensile tests in both directions. Due to the texture, this effect is more pronounced for r_{90} which results in a wider spread between r_0 and r_{90} obtained from the simulations. It can be concluded that effective properties like the plastic strain ratios depend on the mechanical phase contrast. It is therefore important to model the material behavior of the individual phases with sufficient accuracy. Experimental methods like diffraction techniques [9] or micropillar compression tests [54, 10] have been used to determine the phase-specific behavior in dual-phase steels. Such approaches can be used to facilitate a more detailed material modeling although a high experimental effort is required. On the other hand, the dependence of the r-values on the mechanical phase contrast might be exploited to improve the inverse fitting procedure using macroscopic tensile tests as described in this work.



(a)



(b)

Figure 16: Variation of the mechanical phase contrast. Effect on (a) the partitioning of the stress and strain in tensile direction and (b) the predicted r-values for simulations using SMM-1-CP. The strength of the martensite particles was varied by using different values for the carbon content $C^{(m)}$ in Eq. (5).

6. Conclusions

A numerical homogenization scheme based on full-field finite element simulations was applied to study the mechanical behavior of a dual-phase steel microstructure. The effective stress-strain curves and the r -values evaluated from numerical tensile tests in different directions depend on the shape of the martensite particles if the volume content, the spatial distribution and the strength of the martensite phase are constant. A reconstruction procedure based on microstructural correlation functions was successfully applied to generate microstructure models with a martensite morphology that is statistically equivalent to the DP600 investigated in this work. The accuracy of the predicted macroscopic response strongly depends on the microstructural features that are considered in the full-field simulations. In order to predict the plastic flow behavior of the real material, a statistically equivalent martensite morphology and the crystallographic texture have to be included in the microstructure representation. Omitting the influence of the crystallographic texture resulted in a wrong prediction of the r -values. At the same time, the micromechanical fields depend on the chosen constitutive description used for the ferrite matrix which is important if the effect of local damage initiation on the macroscopic response is included in the modeling approach. In addition, the mechanical phase contrast has been identified to influence the plastic strain ratios even if the same effective stress-strain curve is predicted. The applied method is a very flexible approach to study the behavior of dual-phase steels. However, simplified representations of microstructural features and constitutive models that are often found in the literature have to be critically assessed with respect to their predictive capabilities when

used in a virtual testing framework.

7. Acknowledgement

This study was part of the Research Training Group 1483, which is supported by the German Research Foundation (DFG). The authors thank the Institute of Engineering Mechanics (Chair for Continuum Mechanics, KIT) and René Sebastiano, Florian Rieger, Barthel Brylka as well as the Institute for Applied Materials IAM-WK (KIT) and Simone Schuster for providing experimental data used in this work.

- [1] O. Bouaziz, H. Zurob, M. Huang, Driving Force and Logic of Development of Advanced High Strength Steels for Automotive Applications, *Steel Research International* 84 (2013) 937–947, ISSN 16113683.
- [2] C. C. Tasan, M. Diehl, D. Yan, M. Bechtold, F. Roters, L. Schemmann, C. Zheng, N. Peranio, D. Ponge, M. Koyama, K. Tsuzaki, D. Raabe, An Overview of Dual-Phase Steels: Advances in Microstructure-Oriented Processing and Micromechanically Guided Design, *Annual Review of Materials Research* 45 (2015) 391–431, ISSN 1531-7331.
- [3] S. Sodjit, V. Uthaisangsuk, Microstructure based prediction of strain hardening behavior of dual phase steels, *Materials & Design* 41 (2012) 370–379, ISSN 02613069.
- [4] S. K. Paul, A. Kumar, Micromechanics based modeling to predict flow behavior and plastic strain localization of dual phase steels, *Computational Materials Science* 63 (2012) 66–74, ISSN 0927-0256.
- [5] A. Ramazani, K. Mukherjee, H. Quade, U. Prah, W. Bleck, Correlation between 2D and 3D flow curve modelling of DP steels using a microstructure-based RVE approach, *Materials Science and Engineering: A* 560 (2013) 129–139, ISSN 09215093.
- [6] A. Govik, R. Rentmeester, L. Nilsson, A study of the unloading behaviour of dual phase steel, *Materials Science and Engineering: A* 602 (2014) 119–126, ISSN 09215093.
- [7] J. Kadkhodapour, A. Butz, S. Ziaei-Rad, S. Schmauder, A micro mechanical study on failure initiation of dual phase steels under tension

- using single crystal plasticity model, *International Journal of Plasticity* 27 (2011) 1103–1125, ISSN 07496419.
- [8] J. H. Kim, D. Kim, F. Barlat, M.-G. Lee, Crystal plasticity approach for predicting the Bauschinger effect in dual-phase steels, *Materials Science and Engineering: A* 539 (2012) 259–270, ISSN 09215093.
- [9] W. Woo, V. T. Em, E.-Y. Kim, S. H. Han, Y. S. Han, S.-H. Choi, Stress-strain relationship between ferrite and martensite in a dual-phase steel studied by in situ neutron diffraction and crystal plasticity theories, *Acta Materialia* 60 (2012) 6972–6981, ISSN 13596454.
- [10] P. Chen, H. Ghassemi-Armaki, S. Kumar, A. Bower, S. Bhat, S. Sadagopan, Microscale-calibrated modeling of the deformation response of dual-phase steels, *Acta Materialia* 65 (2014) 133–149, ISSN 13596454.
- [11] C. C. Tasan, J. P. M. Hoefnagels, M. Diehl, D. Yan, F. Roters, D. Raabe, Strain localization and damage in dual phase steels investigated by coupled in-situ deformation experiments and crystal plasticity simulations, *International Journal of Plasticity* 63 (2014) 198–210, ISSN 07496419.
- [12] J. Kadkhodapour, S. Schmauder, D. Raabe, S. Ziaei-Rad, U. Weber, M. Calcagnotto, Experimental and numerical study on geometrically necessary dislocations and non-homogeneous mechanical properties of the ferrite phase in dual phase steels, *Acta Materialia* 59 (2011) 4387–4394, ISSN 13596454.

- [13] Q. Han, A. Asgari, P. D. Hodgson, N. Stanford, Strain partitioning in dual-phase steels containing tempered martensite, *Materials Science and Engineering: A* 611 (2014) 90–99, ISSN 09215093.
- [14] A. Ramazani, K. Mukherjee, U. Prah, W. Bleck, Modelling the effect of microstructural banding on the flow curve behaviour of dual-phase (DP) steels, *Computational Materials Science* 52 (2012) 46–54, ISSN 09270256.
- [15] J. Zhou, A. M. Gokhale, A. Gurumurthy, S. P. Bhat, Realistic microstructural RVE-based simulations of stress-strain behavior of a dual-phase steel having high martensite volume fraction, *Materials Science and Engineering: A* 630 (2015) 107–115, ISSN 09215093.
- [16] D. Brands, D. Balzani, L. Scheunemann, J. Schröder, H. Richter, D. Raabe, Computational modeling of dual-phase steels based on representative three-dimensional microstructures obtained from EBSD data, *Archive of Applied Mechanics* 86 (2016) 575–598, ISSN 0939-1533.
- [17] M. Kraska, M. Doig, D. Tikhomirov, D. Raabe, F. Roters, Virtual material testing for stamping simulations based on polycrystal plasticity, *Computational Materials Science* 46 (2009) 383–392, ISSN 09270256.
- [18] M. Baiker, D. Helm, A. Butz, Determination of Mechanical Properties of Polycrystals by Using Crystal Plasticity and Numerical Homogenization Schemes, *Steel Research International* 85 (2014) 988–998, ISSN 16113683.

- [19] H. Zhang, M. Diehl, F. Roters, D. Raabe, A virtual laboratory using high resolution crystal plasticity simulations to determine the initial yield surface for sheet metal forming operations, *International Journal of Plasticity* 80 (2016) 111–138, ISSN 07496419.
- [20] R. Padmanabhan, A. J. Baptista, M. C. Oliveira, L. F. Menezes, Effect of anisotropy on the deep-drawing of mild steel and dual-phase steel tailor-welded blanks, *Journal of Materials Processing Technology* 184 (2007) 288–293.
- [21] M. Firat, A finite element modeling and prediction of stamping formability of a dual-phase steel in cup drawing, *Materials & Design* 34 (2012) 32–39, ISSN 02613069.
- [22] D. Kim, M.-G. Lee, C. Kim, M. L. Wenner, R. H. Wagoner, F. Barlat, K. Chung, J. R. Youn, T. J. Kang, Measurements of Anisotropic Yielding, Bauschinger and Transient Behavior of Automotive Dual-Phase Steel Sheets, *Metals and Materials International* 9 (2003) 561–570, ISSN 1598-9623.
- [23] H. Livatyali, M. Firat, B. Gurler, M. Ozsoy, An experimental analysis of drawing characteristics of a dual-phase steel through a round drawbead, *Materials & Design* 31 (2010) 1639–1643, ISSN 02613069.
- [24] W.-R. Wang, C.-W. He, Z.-H. Zhao, X.-C. Wei, The limit drawing ratio and formability prediction of advanced high strength dual-phase steels, *Materials & Design* 32 (2011) 3320–3327, ISSN 02613069.

- [25] T. Carvalho Resende, S. Bouvier, F. Abed-Meraim, T. Balan, S.-S. Sablin, Dislocation-based model for the prediction of the behavior of b.c.c. materials - Grain size and strain path effects, *International Journal of Plasticity* 47 (2013) 29–48, ISSN 07496419.
- [26] H. Hu, Studies on the Development of High-Strength Dual-Phase Steel Sheets with High r_{m} Values, *Metallurgical Transactions A* 13 (1982) 1257–1262.
- [27] C. Mapelli, S. Barella, R. Venturini, Characterization of the Relation among the Mechanical Behavior and the Texture Features in High Martensitic Dual Phase Steels, *ISIJ International* 45 (2005) 1727–1735.
- [28] S.-H. Han, S.-H. Choi, J.-K. Choi, H.-G. Seong, I.-B. Kim, Effect of hot-rolling processing on texture and r -value of annealed dual-phase steels, *Materials Science and Engineering: A* 527 (2010) 1686–1694, ISSN 09215093.
- [29] M. Delincé, Y. Bréchet, J. D. Embury, M. G. D. Geers, P. J. Jacques, T. Pardoen, Structure-property optimization of ultrafine-grained dual-phase steels using a microstructure-based strain hardening model, *Acta Materialia* 55 (2007) 2337–2350, ISSN 13596454.
- [30] A.-P. Pierman, O. Bouaziz, T. Pardoen, P. J. Jacques, L. Brassart, The influence of microstructure and composition on the plastic behaviour of dual-phase steels, *Acta Materialia* 73 (2014) 298–311, ISSN 13596454.
- [31] S. Y. P. Allain, O. Bouaziz, I. Pushkareva, C. P. Scott, Towards the microstructure design of DP steels: A generic size-sensitive mean-field

- mechanical model, *Materials Science and Engineering: A* 637 (2015) 222–234, ISSN 09215093.
- [32] C. L. Y. Yeong, S. Torquato, Reconstructing random media, *Physical Review E* 57 (1998) 495–506, ISSN 1063-651X.
- [33] C. L. Y. Yeong, S. Torquato, Reconstructing random media. II. Three-dimensional media from two-dimensional cuts, *Physical Review E* 58 (1998) 224–233.
- [34] F. Bachmann, R. Hielscher, H. Schaeben, Texture Analysis with MTEX - Free and Open Source Software Toolbox, *Solid State Phenomena* 160 (2010) 63–68, ISSN 1662-9779.
- [35] R. Sebastiano, Experimentelle und numerische Untersuchung von Dualphasenstahl unter biaxialer Belastung, B.Sc. thesis, Karlsruhe Institute of Technology, Institute of Engineering Mechanics - Chair for Continuum Mechanics, 2015.
- [36] H. Kumar, C. L. Briant, W. A. Curtin, Using microstructure reconstruction to model mechanical behavior in complex microstructures, *Mechanics of Materials* 38 (2006) 818–832, ISSN 01676636.
- [37] S. Torquato, *Random Heterogeneous Materials: Microstructure and Macroscopic Properties*, Springer, New York, 2002.
- [38] M. A. Groeber, M. A. Jackson, DREAM.3D: A Digital Representation Environment for the Analysis of Microstructure in 3D, *Integrating Materials and Manufacturing Innovation* 3 (2014) 1–17.

- [39] P. Eisenlohr, F. Roters, Selecting a set of discrete orientations for accurate texture reconstruction, *Computational Materials Science* 42 (2008) 670–678, ISSN 09270256.
- [40] Abaqus, Abaqus Manuals, v6.13. Dassault Systèmes Simulia Corp., Providence, RI, USA., 2013.
- [41] R. Rodriguez, I. Gutiérrez, Unified Formulation to Predict the Tensile Curves of Steels with Different Microstructures, *Materials Science Forum* 426-432 (2003) 4525–4530, ISSN 1662-9752.
- [42] A. Ramazani, K. Mukherjee, A. Schwedt, P. Goravanchi, U. Prahl, W. Bleck, Quantification of the effect of transformation-induced geometrically necessary dislocations on the flow-curve modelling of dual-phase steels, *International Journal of Plasticity* 43 (2013) 128–152, ISSN 07496419.
- [43] Y. Bergström, Y. Granbom, D. Sterkenburg, A Dislocation-Based Theory for the Deformation Hardening Behavior of DP Steels: Impact of Martensite Content and Ferrite Grain Size, *Journal of Metallurgy* 2010 (2010) 1–16, ISSN 1687-9465.
- [44] S. R. Kalidindi, C. A. Bronkhorst, L. Anand, Crystallographic Texture Evolution in Bulk Deformation Processing of FCC Metals, *Journal of the Mechanics and Physics of Solids* 40 (1992) 537–569.
- [45] W. M. Haynes, CRC Handbook of Chemistry and Physics, 96th Edition (Internet Version 2016), CRC Press/Taylor and Francis, Boca Raton, 2016.

- [46] I. Schmidt, Numerical homogenisation of an elasto-plastic model-material with large elastic strains: Macroscopic yield surfaces and the Eulerian normality rule, *Computational Mechanics* 48 (2011) 579–590, ISSN 0178-7675.
- [47] S. Sun, M. Pugh, Properties of thermomechanically processed dual-phase steels containing fibrous martensite, *Materials Science and Engineering: A* 335 (2002) 298–308, ISSN 09215093.
- [48] M. Sarwar, R. Priestner, Influence of ferrite-martensite microstructural morphology on tensile properties of dual-phase steel, *Journal of Materials Science* 31 (1996) 2091–2095.
- [49] S.-H. Choi, E.-Y. Kim, W. Woo, S. H. Han, J. H. Kwak, The effect of crystallographic orientation on the micromechanical deformation and failure behaviors of DP980 steel during uniaxial tension, *International Journal of Plasticity* 45 (2013) 85–102, ISSN 07496419.
- [50] N. Vajragupta, P. Wechsuanmanee, J. Lian, M. Sharaf, S. Münstermann, A. Ma, A. Hartmaier, W. Bleck, The modeling scheme to evaluate the influence of microstructure features on microcrack formation of DP-steel: The artificial microstructure model and its application to predict the strain hardening behavior, *Computational Materials Science* 94 (2014) 198–213, ISSN 09270256.
- [51] V. H. Baltazar Hernandez, S. K. Panda, M. L. Kuntz, Y. Zhou, Nanoinindentation and microstructure analysis of resistance spot welded dual phase steel, *Materials Letters* 64 (2010) 207–210, ISSN 0167577X.

- [52] K. Hayashi, K. Miyata, F. Katsuki, T. Ishimoto, T. Nakano, Individual mechanical properties of ferrite and martensite in Fe-0.16mass% C-1.0mass% Si-1.5mass% Mn steel, *Journal of Alloys and Compounds* 577 (2013) 593–596, ISSN 09258388.
- [53] H. Li, S. Gao, Y. Tian, D. Terada, A. Shibata, N. Tsuji, Influence of tempering on mechanical properties of ferrite and martensite dual phase steel, *Materials Today: Proceedings* 2S (2015) 667–671.
- [54] H. Ghassemi-Armaki, R. Maaß, S. P. Bhat, S. Sriram, J. R. Greer, K. S. Kumar, Deformation response of ferrite and martensite in a dual-phase steel, *Acta Materialia* 62 (2014) 197–211, ISSN 13596454.